CHINESE OPTICS LETTERS
Vol. 20, No. 10 | October 2022

Broadband angular momentum cascade via a multifocal graphene vortex generator

Zhongwei Jin (金中薇)[1,2,†], Guiyuan Cao (曹桂源)[3,†], Hongtao Wang (王洪涛)[2], Han Lin (林 翰)[3,4], Baohua Jia (贾宝华)[3,4,5*], and Cheng-Wei Qiu (仇成伟)[2**]

[1] College of Optical and Electronic Technology, China Jiliang University, Hangzhou 310018, China

[2] Department of Electrical and Computer Engineering, National University of Singapore, Singapore 117583, Singapore

[3] Centre of Translational Atomaterials (CTAM), Faculty of Science, Engineering and Technology, Swinburne University of Technology, Hawthorn, VIC 3122, Australia

[4] School of Science, RMIT University, Melbourne, VIC 3000, Australia

[5] The Australian Research Council (ARC) Industrial Transformation Training Centre in Surface Engineering for Advanced Materials (SEAM), Swinburne University of Technology, Hawthorn, VIC 3122, Australia

*Corresponding author: bjia@swin.edu.au

**Corresponding author: chengwei.qiu@nus.edu.sg

Received June 5, 2022 | Accepted June 20, 2022 | Posted Online July 6, 2022

Light beams carrying orbital angular momentum (OAM) have inspired various advanced applications, and such abundant practical applications in turn demand complex generation and manipulation of optical vortices. Here, we propose a multifocal graphene vortex generator, which can produce broadband angular momentum cascade containing continuous integer non-diffracting vortex modes. Our device naturally embodies a continuous spiral slit vortex generator and a zone plate, which enables the generation of high-quality continuous vortex modes with deep depths of foci. Meanwhile, the generated vortex modes can be simultaneously tuned through incident wavelength and position of the focal plane. The elegant structure of the device largely improves the design efficiency and can be fabricated by laser nanofabrication in a single step. Moreover, the outstanding property of graphene may enable new possibilities in enormous practical applications, even in some harsh environments, such as aerospace.

Keywords: optical vortex; multifocus; broadband; wavelength tunability; graphene.
DOI: 10.3788/COL202220.103602

1. Introduction

A light beam carrying orbital angular momentum (OAM) with a helical wavefront, which can be represented as $\exp(-il\varphi)$ with a phase singularity in the center, is called an optical vortex[1–3]. The unique optical properties of optical vortices have inspired both fundamental and emerging fascinating applications, such as nano/microparticle trapping[4] and manipulation[5], microscopic imaging[6]. So far, many mature methods have been carried out to produce light with designed OAM modes, such as spatial light modulators, fork gratings[7], spiral phase plates[8], and computer generated holograms[9]. Such traditional devices play significant roles in diverse optical systems. However, these thick and bulky devices are unsuitable for system integration and miniaturization; on the other hand, they either have limited working bandwidth or can only generate vortices with quite limited modes. Recently, the abundant practical applications of optical vortices call for more complex generation and manipulation of vortex beams. For example, under the scenes in which different OAM modes need to be fed into systems within one component[10,11], multiple/continuous ordered vortex beams are demanded; for trapping of tiny particles and stimulated emission depletion microscopy[12], non-diffracting vortex beams are required. Therefore, in this work, we propose a broadband multifocal graphene vortex generator, which can produce broadband angular momentum cascade containing continuous integer non-diffracting vortex modes. Our multifocal graphene vortex generator is composed of a multi-turn spiral slit structure, which naturally embodies a continuous spiral slit vortex generator and a zone plate. Thus, the device enables the generation of broadband high-quality continuous vortex modes with multiple foci of deep depths. Meanwhile, the generated vortex modes can be simultaneously tuned through changing the incident wavelength or position of the focal plane. The elegant structure of our multifocal vortex graphene generator largely improves the design efficiency and can be fabricated using facile laser nanofabrication in a single step[13], which provide possibilities for future scalable production. Moreover, thanks to the exceptional optical properties of grapheme[14], our proposed broadband multifocal vortex generator (BMVG) may provide new possibilities in enormous practical applications such as dark-field imaging, nanoparticle's manipulation, and optical information processing, even in harsh and/or extreme environments[15], such as aerospace applications.

2. Results and Discussion

The distribution of our BMVG can be simply expressed as

$$F(\theta) = \sqrt{r_0^2 + 2l_0 z_0 \lambda_0 \cdot \frac{\theta}{2\pi}},\quad \theta \in [0, M\cdot 2\pi], \quad \left(M \geq 3,\ r_0 \ll \frac{z_0}{b}\right), \tag{1}$$

where θ denotes the azimuthal angle, r_0 denotes the starting radius of the structure, z_0 is the pre-designed focal plane, l_0 is the pre-designed topological charge at focal plane z_0, and λ_0 is the pre-designed working wavelength. Instead of a normal spiral structure where the θ extends from 0 to 2π, we make θ extend from 0 to $M\cdot 2\pi$ ($M \geq 3$) to obtain a multi-turn (M turns) spiral structure, as shown in Fig. 1(a). When dissembling the structure, our BMVG can be expressed as follows:

$$F(\theta) = \sqrt{F_1(\theta)^2 + F_2(\theta)^2}, \qquad \theta \in [0, 2\pi]. \tag{2}$$

Here,

$$F_1(\theta) = \sqrt{N\lambda_0 z_0}, \qquad \theta \in [0, 2\pi], \tag{3}$$

where $N = 2l \cdot (n-1)$, $n = 1, 2, \ldots, M$, and

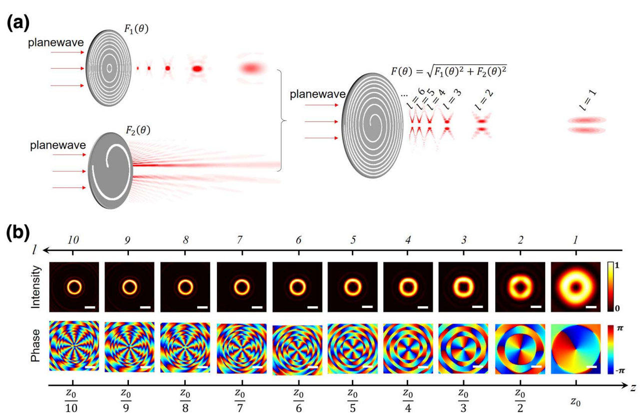

Fig. 1. Concept and working principle of our rGO broadband multifocal vortex generator (BMVG). (a) Schematic of working principle of our BMVG. (b) Simulated intensity and phase profiles of continuous OAM patterns captured at corresponding focal planes. Scale bar, 4 μm.

$$F_2(\theta) = \sqrt{r_0^2 + 2l_0 z_0 \lambda_0 \cdot \frac{\theta}{2\pi}}, \qquad \theta \in [0, 2\pi], \qquad (r_0 \ll z_0). \tag{4}$$

As is shown in Fig. 1(a), the zone plate structure defined by Eq. (3) can generate multiple foci with multiple deep depths of foci (DoFs) at focal planes of $z = z_0/m$, $m = 1, 2, 3, \ldots$, since light penetrating from the ring areas always has constructive interference at $z = z_0/m$, $m = 1, 2, 3, \ldots$, as long as the Fresnel approximation can be satisfied. In the meantime, the Fermat spiral slit structure defined by Eq. (4) can produce a Bessel-like beam carrying a series of continuous OAM modes along the propagation direction, and the topological charges carried by the light beams are inversely proportional to the propagation distance. Since our BMVG possesses the properties of the above two devices simultaneously, our BMVG can produce a series of non-diffracting continuous integer OAMs at $z = z_0$, $z_0/2, \ldots, z_0/m$ with topological charges of $l = l_0, 2l_0, \ldots, ml_0$, $m = 1, 2, \ldots$, respectively.

To illustrate our idea, we design our BMVG according to Eq. (1) by choosing $\lambda_0 = 633\,\text{nm}$, $r_0 = 20\,\mu\text{m}$, $l_0 = 1$, $z_0 = 3600\,\mu\text{m}$, and $M = 8$ as a proof-of-concept example. The slit is set as 0.4 μm considering the balance between fabrication convenience and the device's efficiency while maintaining the phase difference induced by the slit width to be as small as possible. To verify the function of the device, we simulated the intensity and phase profiles of the light field passing through the BMVG in the Fresnel far-field region at $z = z_0/m$, $m = 1, 2, \ldots, 10$, respectively, and the results are shown in Fig. 1(b). According to Fig. 1(b), it can be seen that at the pre-designed focal plane z_0, the intensity profile of the light field shows a "donut" shaped ring, while the phase profile of the light field shows phase change of 2π around the central singularity point; both indicate an OAM mode of $l_0 = 1$. When we capture the light field at $z_0/2$ along the propagation direction, the phase profile together with the intensity profile indicates an OAM mode of $l = 2 = 2l_0$. So on and so forth, we can totally obtain 10 clear OAM modes along the propagation direction. Therefore, such a single device can produce a series of high-quality continuous integer OAMs.

To demonstrate that the generated OAMs from our BMVG have deep DoFs, we simulated the intensity profile of the light field in the x–z plane after our designed BMVG from $z = 300\,\mu\text{m}$ to $z = 4000\,\mu\text{m}$, and the result is shown in Fig. 2(a). It can be seen that due to the conical wavefront induced by the zone plate structure concealed in our device, the light field after our BMVG becomes a continuous variant-order Bessel-like beam, and the modes of each section in the Bessel-like beam, i.e., the non-diffracting region, vary with the propagation distance. In order to explore more details, we extracted every mode in the beam from $l = 1$ to $l = 10$ and showed their zoom-in x–z intensity profiles in Fig. 2(b). When $l = 1$, the non-diffracting region of the beam spans from $z = 3200\,\mu\text{m}$ to $z = 4000\,\mu\text{m}$, which is more than 1260 times the length of λ_0. As the topological charge l increases, the length of the non-diffracting region decreases. But, even at $l = 10$, the non-diffracting region still

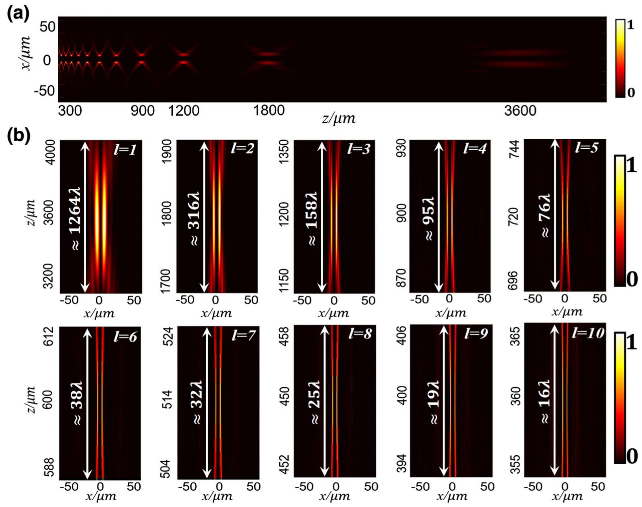

Fig. 2. Simulated light fields of our BMVG in the x–z plane. (a) Simulated intensity profile in the x–z plane of the light field generated by our BMVG. (b) Zoom-in simulated intensity profiles (x–z plane) of the non-diffracting regions of generated OAM modes from $l = 1$ to $l = 10$.

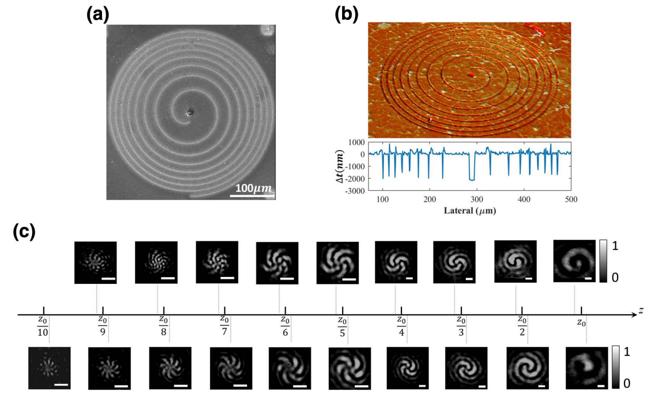

Fig. 3. Fabricated sample and measured results of the BMVG. (a) The scanning electronic microscopy (SEM) image of the entire fabricated sample. (b) The topographic profile (top) of the rGO sample measured by an optical profiler and the cross-sectional profile (bottom) marked by the white dashed line in the top image of (b). (c) The interference patterns of the generated OAMs captured before and after the designed focal planes upon 633 nm illumination. Scale bar, 6 μm.

spans almost 16 times the length of λ_0, which proves that our BMVG can generate continuous high-quality OAMs with long DoFs.

To further verify the function of our device, we experimentally fabricated and characterized the designed BMVG. We fabricated our designed BMVG on a 1-μm-thick reduced graphene oxide (rGO) film[15] so that the film is thick enough to block the impinging light while guaranteeing fabrication convenience using direct laser ablation[16]. In our sample, the slit part is ablated so that incident light can transmit through the slit. In order to read the order of the generated OAMs directly from the measured results, a circular hole with a radius of 10 μm was drilled through the center of the sample, as shown in the scanning electronic microscopy (SEM) image in Fig. 3(a). The total area of the device is within 400 μm × 400 μm. Figure 3(b) shows the topographic profile (top) of our rGO sample measured by an optical profiler and the cross-sectional profile (bottom) marked by the white dashed line in the top image of Fig. 3(b). The Gaussian shaped surface profile is due to the intensity distribution of the laser focal spot during the laser ablation fabrication process. The measurement results confirm that the multi-turn spiral slits are thoroughly ablated through the rGO film.

Figure 3(c) shows a series of interference patterns captured before and after the centers of the non-diffracting regions of different modes. According to the interference patterns, we can directly read the modes of the generated OAMs from the number of arms in the intensity profiles. For each mode, the handedness of the interference patterns before and after the center of the non-diffracting region is opposite. This is because before the beginning of the non-diffracting region of each mode the wavefront of the light wave coming from our designed BMVG is convex [as is shown in Fig. 2(a)]. After the non-diffracting region, it will then diverge, and the wavefront will become concave. Such a phase change in the beam leads to the change of handedness of the interference patterns. But, the handedness of the OAMs never changes during this process. From Fig. 3(c), the interference patterns from $l = 1$ to $l = 9$ can be clearly observed. For $l = 10$, the interference pattern after the center of the non-diffracting region can still be captured, though it is slightly messy. We did not capture the interference pattern of $l = 10$ before the center of the non-diffracting region. This is because when the propagation distance gets too short, the Fresnel approximation cannot be satisfied anymore. Our fabricated BMVG has a diffraction efficiency that varies as the focal position changes. At $z = 3600\,\mu\text{m}$ ($l = 1$), the diffraction efficiency is around 10.53%, and, at $z = 1800\,\mu\text{m}$ ($l = 2$), the diffraction efficiency is around 28.88%. The diffraction efficiency increases as the focal position gets closer to the device. At $z = 360\,\mu\text{m}$ ($l = 10$), the diffraction efficiency is around 65%. We can improve the diffraction efficiency by increasing the number of turns of the spiral and the slit width.

The unique properties of our BMVG also facilitate it to work as a wavelength tunable and focal distance tunable device. Specifically, Eq. (1) can be rewritten in a different formation as

$$F(\theta) = \sqrt{r_0^2 + 2(a \cdot b l_0)\left(\frac{z_0}{a}\right)\left(\frac{\lambda_0}{b}\right) \cdot \frac{\theta}{2\pi}}$$
$$\theta \in [0, M \cdot 2\pi], \qquad \left(M \geq 3, r_0 \ll \frac{z_0}{b}\right), \tag{5}$$

where a and b can be any positive constant as long as $a \cdot b$ is a positive integer, and the corresponding Fresnel approximation can be satisfied. According to Eq. (5), when $a = 1$, our BMVG behaves as a wavelength tunable device. Supposing we change the working wavelength from λ_0 to λ_0/b, we can obtain an

OAM with mode $l = bl_0$ at the focal plane of $z = z_0$. It means that at a fixed position, when we change the illumination wavelength, different modes can be obtained at the corresponding focal plane. Similarly, when $b = 1$, our BMVG becomes a focal distance tunable device. It means that under the same working wavelength, we can achieve different OAM modes at different positions, which has already been demonstrated in the first part of this manuscript. Finally, when $a \neq 1$ and $b \neq 1$, but $a \cdot b$ maintains a positive integer, under the required approximate condition, we can get an OAM mode of $l = a \cdot b$ at focal plane $z = z_0/a$ under the working wavelength λ_0/b. This indicates that the device can be tuned by wavelength and focal distance simultaneously. Moreover, the slit structure enables our device to work under a broadband range, which extends from visible to near-infrared. To demonstrate this capability, we tested our device at several wavelengths with both simulation and measurement. The results are provided in Fig. 4 as proof-of-concept examples.

First of all, we tested the wavelength tunability of the device. We fixed the test position before the focal plane at $z = 514\ \mu m$ and changed the illuminating wavelengths from 886 nm, 739 nm to 633 nm. As a result, a series of different modes from $l = 5$ to $l = 7$ can be obtained at the same measured position. The simulated and measured intensity profiles captured before and after the center of the non-diffracting region are provided in Fig. 4(a). Next, to demonstrate that our device can be tuned simultaneously by both wavelength and focal distance, we randomly selected some working wavelengths and captured the same mode of $l = 6$ near the corresponding focal positions. The working wavelengths we chose here are 633 nm, 760 nm, 800 nm, 850 nm, 886 nm, 900 nm, and 1000 nm. Their relative focal positions of $l = 6$ are 720 μm, 600 μm, 570 μm, 536 μm, 514 μm, 506 μm, and 456 μm, respectively. The measured interference patterns are shown in Fig. 4(b), which proved that our BMVG can be simultaneously tuned by the wavelength and focal position. The above simulated and measured results span from visible to near-infrared. To further prove that our device can finely work in the near-infrared region, we tested our device at the working wavelength of 900 nm and obtained continuous interference OAM patterns from $l = 1$ to 9, both before and after the focal planes. The results are shown in Fig. 4(c). The results presented in Fig. 4 well proved the multi-dimensional tunability of the proposed device.

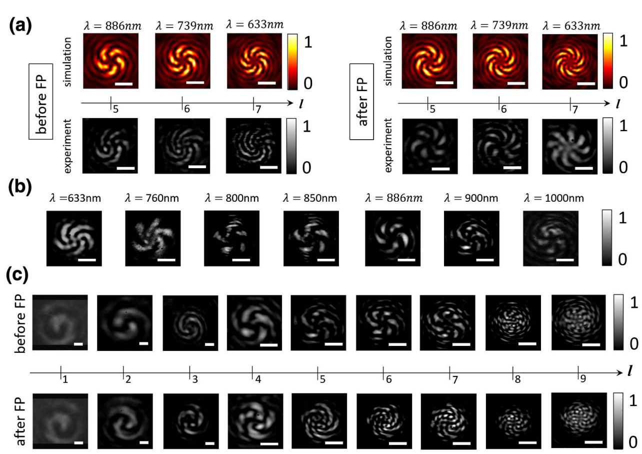

Fig. 4. Demonstration of wavelength tunability and focal distance tunability of our BMVG. (a) Simulated and measured interference patterns of generated OAMs captured before (left panel) and after (right panel) $z = 450\ \mu m$ under the incident light of 886 nm, 739 nm, and 633 nm. Scale bar, 6 μm. (b) The measured interference patterns of the generated OAMs under 633 nm (near $z = 720\ \mu m$), 760 nm (near $z = 600\ \mu m$), 800 nm (near $z = 570\ \mu m$), 850 nm (near $z = 536\ \mu m$), 886 nm (near $z = 514\ \mu m$), 900 nm (near $z = 506\ \mu m$), and 1000 nm (near $z = 456\ \mu m$). Scale bar, 6 μm. (c) The measured interference patterns of the generated OAMs captured before and after the designed focal planes upon 900 nm illumination. Scale bar, 6 μm.

3. Conclusion

In conclusion, we proposed a multi-turn spiral slit structure, which naturally embodies the structure of a continuous spiral slit vortex generator and a zone plate. Such a device can work as a broadband multifocal continuous vortex generator. We prove the function of our device with rigorous mathematical language and completely consistent simulation and experimental results. Compared with previous similar devices, our BMVG can work with both linearly polarized light and circularly polarized light at different wavelengths. In addition, it can be fabricated by a simple and scalable laser nanofabrication method and takes much less fabrication time. The flexibility of our design enables it to work under a broadband spectrum while working as a wavelength tunable and focal position tunable device. However, our device's efficiency is low since a majority of the incident light is blocked by the rGO film. Nevertheless, overall, we believe the multi-functionalities and tuning flexibility of our graphene BMVG provide a new avenue for next generation scalable OAM generators.

4. Methods

Simulation: The simulation of this work is based on the Fresnel diffraction theory and the codes are implemented on MATLAB on a personal computer.

Fabrication: A 1-μm-thick graphene oxide (GO) film fabricated by the vacuum filtration method[17–19] using aqueous GO solution is attached to a cover glass substrate. The aqueous GO dispersion was synthesized by chemical oxidization of graphite via the modified Hummers method.

The vortex graphene generator is fabricated in one step by a commercial laser nanoprinting setup (Special Edition, Nanoprint3D from Innofocus Photonics Technology Pty. Ltd.) with a femtosecond laser (Libra, 800 nm wavelength, 100 fs pulse, 10 kHz repetition rate). The computer-controlled system was used to control the parameters of the laser ablation process, including exposure time, laser power, scanning speed, and patterns. The scanning speed was 100 μm/s to ensure a smooth line fabrication. The laser focal spot has a full-width at half-maximum (FWHM) of 600 nm for presenting high resolution. The laser power is 100 μW.

Optical characterization: The focusing performance of the graphene generator is characterized by a home-made imaging system, which uses a $4f$ system composed of an objective lens and a tube lens. The focusing intensity distribution is recorded by a CCD camera (Watec 902H). The graphene generator is mounted on a scanning stage, which can move along the z axis. A commercial supercontinuum laser source (NKT Photonics, SuperK Flanium) was used to illuminate the graphene generator.

Acknowledgement

C.-W. Qiu acknowledges the support from Advanced Research and Technology Innovation Centre (ARTIC) in National University of Singapore (R-261-518-004-720 | A-0005947-16-00). B. Jia and H. Lin acknowledge the Australia Research Council through the Discovery Project Scheme (DP190103186, DP220100603, and FT210100806) and the Industrial Transformation Training Centre Scheme (IC180100005).

†These authors contributed equally to this work.

References

1. H. Sroor, Y.-W. Huang, B. Sephton, D. Naidoo, A. Vallés, V. Ginis, C.-W. Qiu, A. Ambrosio, F. Capasso, and A. Forbes, "High-purity orbital angular momentum states from a visible metasurface laser," Nat. Photonics **14**, 498 (2020).
2. C. Huang, C. Zhang, S. Xiao, Y. Wang, Y. Fan, Y. Liu, N. Zhang, G. Qu, H. Ji, J. Han, L. Ge, Y. Kivshar, and Q. Song, "Ultrafast control of vortex microlasers," Science **367**, 1018 (2020).
3. Z. Jin, D. Janoschka, J. Deng, L. Ge, P. Dreher, B. Frank, G. Hu, J. Ni, Y. Yang, J. Li, C. Yu, D. Lei, G. Li, S. Xiao, S. Mei, H. Giessen, F. Meyer zu Heringdorf, and C.-W. Qiu, "Phyllotaxis-inspired nanosieves with multiplexed orbital angular momentum," eLight **1**, 5 (2021).
4. S. Mei, K. Huang, T. Zhang, M. Qasim Mehmood, H. Liu, C. T. Lim, J. Teng, and C.-W. Qiu, "Evanescent vortex: optical subwavelength spanner," Appl. Phys. Lett. **109**, 191107 (2016).
5. Y. Shen, X. Wang, Z. Xie, C. Min, X. Fu, Q. Liu, M. Gong, and X. Yuan, "Optical vortices 30 years on: OAM manipulation from topological charge to multiple singularities," Light Sci. Appl. **8**, 90 (2019).
6. G. Chen, Z.-Q. Wen, and C.-W. Qiu, "Superoscillation: from physics to optical applications," Light Sci. Appl. **8**, 56 (2019).
7. R. Zeng, Q. Zhao, Y. Shen, Y. Liu, and Y. Yang, "Structural stability of open vortex beams," Appl. Phys. Lett. **119**, 171105 (2021).
8. Q. Zhou, M. Liu, W. Zhu, L. Chen, Y. Ren, H. J. Lezec, Y. Lu, A. Agrawal, and T. Xu, "Generation of perfect vortex beams by dielectric geometric metasurface for visible light," Laser Photonics Rev. **15**, 2100390 (2021).
9. N. Zhou, S. Zheng, X. Cao, Y. Zhao, S. Gao, Y. Zhu, M. He, X. Cai, and J. Wang, "Ultra-compact broadband polarization diversity orbital angular momentum generator with $3.6 \times 3.6\ \mu m^2$ footprint," Sci. Adv. **5**, eaau9593 (2019).
10. L. Jin, Y.-W. Huang, Z. Jin, R. C. Devlin, Z. Dong, S. Mei, M. Jiang, W. T. Chen, Z. Wei, H. Liu, J. Teng, A. Danner, X. Li, S. Xiao, S. Zhang, C. Yu, J. K. W. Yang, F. Capasso, and C.-W. Qiu, "Dielectric multi-momentum meta-transformer in the visible," Nat. Commun. **10**, 4789 (2019).
11. Y. Yang, L. Wu, Y. Liu, D. Xie, Z. Jin, J. Li, G. Hu, and C.-W. Qiu, "Deuterogenic plasmonic vortices," Nano Lett. **20**, 6774 (2020).
12. S. Mei, M. Q. Mehmood, S. Hussain, K. Huang, X. Ling, S. Y. Siew, H. Liu, J. Teng, A. Danner, and C.-W. Qiu, "Flat helical nanosieves," Adv. Funct. Mater. **26**, 5255 (2016).
13. H. Lin, B. Jia, and M. Gu, "Dynamic generation of Debye diffraction-limited multifocal arrays for direct laser printing nanofabrication," Opt. Lett. **36**, 406 (2011).
14. Y. Yang, H. Lin, B. Y. Zhang, Y. Zhang, X. Zheng, A. Yu, M. Hong, and B. Jia, "Graphene-based multilayered metamaterials with phototunable architecture for on-chip photonic devices," ACS Photonics **6**, 1033 (2019).
15. G. Cao, H. Lin, S. Fraser, X. Zheng, B. Del Rosal, Z. Gan, S. Wei, X. Gan, and B. Jia, "Resilient graphene ultrathin flat lens in aerospace, chemical, and biological harsh environments," ACS Appl. Mater. Interfaces **11**, 20298 (2019).
16. H. Lin, B. C. P. Sturmberg, K.-T. Lin, Y. Yang, X. Zheng, T. K. Chong, C. M. de Sterke, and B. Jia, "90-nm-thick graphene metamaterial for strong and extremely broadband absorption of unpolarized light," Nat. Photonics **13**, 270 (2019).
17. X. Zheng, B. Xu, S. Li, H. Lin, L. Qiu, D. Li, and B. Jia, "Free-standing graphene oxide mid-infrared polarizers," Nanoscale **12**, 11480 (2020).
18. X. Zheng, B. Jia, H. Lin, L. Qiu, D. Li, and M. Gu, "Highly efficient and ultra-broadband graphene oxide ultrathin lenses with three-dimensional subwavelength focusing," Nat. Commun. **6**, 8433 (2015).
19. H. Wang, C. Hao, H. Lin, Y. Wang, T. Lan, C.-W. Qiu, and B. Jia, "Generation of super-resolved optical needle and multifocal array using graphene oxide metalenses," Opto-Electron. Adv. **4**, 02200031 (2021).